Contents lists available at ScienceDirect

Nuclear Instruments and Methods in Physics Research A

FADC signal reconstruction for the MAGIC telescope

J. Albert [a], E. Aliu [b], H. Anderhub [c], P. Antoranz [d], A. Armada [b], M. Asensio [d], C. Baixeras [b], J.A. Barrio [d], H. Bartko [f,*], D. Bastieri [g], J. Becker [h], W. Bednarek [i], K. Berger [a], C. Bigongiari [g], A. Biland [c], R.K. Bock [f,g], P. Bordas [j], V. Bosch-Ramon [j], T. Bretz [a], I. Britvitch [c], M. Camara [d], E. Carmona [f], A. Chilingarian [k], S. Ciprini [l], J.A. Coarasa [f], S. Commichau [c], J.L. Contreras [d], J. Cortina [b], M.T. Costado [m,v], V. Curtef [h], V. Danielyan [k], F. Dazzi [g], A. De Angelis [n], C. Delgado [m], R. de los Reyes [d], B. De Lotto [n], E. Domingo-Santamaría [b], D. Dorner [a], M. Doro [g], M. Errando [b], M. Fagiolini [o], D. Ferenc [p], E. Fernández [b], R. Firpo [b], J. Flix [b], M.V. Fonseca [d], L. Font [e], M. Fuchs [f], N. Galante [f], R.J. García-López [m,v], M. Garczarczyk [f], M. Gaug [m,*], M. Giller [i], F. Goebel [f], D. Hakobyan [k], M. Hayashida [f], T. Hengstebeck [q], A. Herrero [m,v], D. Höhne [a], J. Hose [f], C.C. Hsu [f], P. Jacon [i], T. Jogler [f], R. Kosyra [f], D. Kranich [c], R. Kritzer [a], A. Laille [p], E. Lindfors [l], S. Lombardi [g], F. Longo [n], J. López [b], M. López [d], E. Lorenz [c,f], P. Majumdar [f], G. Maneva [r], K. Mannheim [a], O. Mansutti [n], M. Mariotti [g], M. Martínez [b], D. Mazin [b], C. Merck [f], M. Meucci [o], M. Meyer [a], J.M Miranda [d], R. Mirzoyan [f], S. Mizobuchi [f], A. Moralejo [b], D. Nieto [d], K. Nilsson [l], J. Ninkovic [f], E. Oña-Wilhelmi [b], N. Otte [f,q], I. Oya [d], M. Panniello [m,1], R. Paoletti [o], J.M. Paredes [j], M. Pasanen [l], D. Pascoli [g], F. Pauss [c], R. Pegna [o], M. Persic [n,s], L. Peruzzo [g], A. Piccioli [o], N. Puchades [b], E. Prandini [g], A. Raymers [k], W. Rhode [h], M. Ribó [j], J. Rico [b], M. Rissi [c], A. Robert [e], S. Rügamer [a], A. Saggion [g], T. Saito [f], A. Sánchez [e], P. Sartori [g], V. Scalzotto [g], V. Scapin [n], R. Schmitt [a], T. Schweizer [f], M. Shayduk [q,f], K. Shinozaki [f], S.N. Shore [t], N. Sidro [b], A. Sillanpää [l], D. Sobczynska [i], A. Stamerra [o], L.S. Stark [c], L. Takalo [l], P. Temnikov [r], D. Tescaro [b], M. Teshima [f], D.F. Torres [u], N. Turini [o], H. Vankov [r], V. Vitale [n], R.M. Wagner [f], T. Wibig [i], W. Wittek [f], F. Zandanel [g], R. Zanin [b], J. Zapatero [e]

[a] Universität Würzburg, D-97074 Würzburg, Germany
[b] Institut de Fí sica d'Altes Energies, Edifici Cn., E-08193 Bellaterra (Barcelona), Spain
[c] ETH Zurich, CH-8093 Zurich, Switzerland
[d] Universidad Complutense, E-28040 Madrid, Spain
[e] Universitat Autònoma de Barcelona, E-08193 Bellaterra, Spain
[f] Max-Planck-Institut für Physik, D-80805 München, Germany
[g] Università di Padova and INFN, I-35131 Padova, Italy
[h] Universität Dortmund, D-44227 Dortmund, Germany
[i] University of Łódź, PL-90236 Lodz, Poland
[j] Universitat de Barcelona, E-08028 Barcelona, Spain
[k] Yerevan Physics Institute, AM-375036 Yerevan, Armenia
[l] Tuorla Observatory, FI-21500 Piikkiö, Finland
[m] Inst. de Astrofisica de Canarias, E-38200 La Laguna, Tenerife, Spain
[n] Università di Udine and INFN Trieste, I-33100 Udine, Italy
[o] Università di Siena and INFN Pisa, I-53100 Siena, Italy
[p] University of California, Davis, CA 95616-8677, USA
[q] Humboldt-Universität zu Berlin, D-12489 Berlin, Germany
[r] Institute for Nuclear Research and Nuclear Energy, BG-1784 Sofia, Bulgaria
[s] INAF/Osservatorio Astronomico and INFN Trieste, I-34131 Trieste, Italy
[t] Università di Pisa and INFN Pisa, I-56126 Pisa, Italy
[u] ICREA & Institut de Ciències de l'Espai (CSIC-IEEC), E-08193 Bellaterra, Spain
[v] Depto. de Astrofisica, Universidad, E-38206 La Laguna, Tenerife, Spain

* Corresponding authors. Tel.: +49 89 32354 259.
  E-mail addresses: hbartko@mppmu.mpg.de (H. Bartko), markus@iac.es (M. Gaug).
  [1] Deceased.

A R T I C L E   I N F O

A B S T R A C T

Until April 2007 the Major Atmospheric Gamma ray Imaging Cherenkov (MAGIC) telescope used a 300 MSamples/s flash analog-to-digital converter (FADC) system to sample the shaped photomultiplier tube (PMT) signals produced by the captured Cherenkov photons of air showers. Different algorithms to reconstruct the signal from the read-out samples (extractors) have been implemented and are described and compared. Criteria based on the obtained charge and time resolution/bias are defined and used to judge the different extractors, by applying them to calibration, cosmic and pedestal signals. The achievable charge and time resolution have been derived as functions of the number of incident photo-electrons.

1. Introduction

The Major Atmospheric Gamma ray Imaging Cherenkov (MAGIC) telescope [1] uses the IACT technique [2] to study the very high energy (VHE, $E > 50\,\text{GeV}$) γ-ray emission from astrophysical sources, at the lowest possible energy threshold. The technique uses Cherenkov radiation: A VHE γ-ray entering the earth's atmosphere initiates a shower (cascade) of electrons and positrons, with a particle density maximum about 10 km above sea level (for an energy of 1 TeV). The particles in the cascade produce Cherenkov light in a cone of about $1°$ half-angle, which illuminates an area of around 120 m radius on the ground. If the MAGIC telescope is located in this area, part of the Cherenkov light will be collected by the telescope mirrors and a shower image will be projected onto the photomultiplier tube (PMT) camera. The Cherenkov photons arrive within a very short time interval of a few nanoseconds at the telescope camera, whose pixels are fast light sensors such as PMTs, so that one can trigger on the coincident light signals. The fluctuations of the light of the night sky (LONS) cause background noise. This effect is minimized by using low exposure times (signal integration times), typically of the order of 10 ns. To reach the highest sensitivity and the lowest energy threshold, the recorded signals have to be accurately reconstructed. Two quantities are of interest: the total signal charge and the signal arrival time. The signal charge (the total number of photo-electrons released from the photocathode of the PMT) is proportional to the total area below the pulse. The sum of the signal charges of all camera pixels is a measure of the shower energy. The signal arrival time is given by the time difference between the first recorded flash analog-to-digital converter (FADC) sample and a characteristic position on the pulse shape, like the maximum, the half-maximum on the rising edge or the center of gravity of the pulse. The timing information may be used to discriminate between pixels whose signals belong to the shower, and pixels which are affected by randomly timed background noise. The pixels with a low signal-to-noise ratio are rejected for the subsequent image parameterization [3,4].

The main background to γ-rays originates from the much more frequent showers induced by isotropic hadronic cosmic rays. Monte Carlo (MC) based simulations predict different time structures for γ-ray and hadron induced shower images as well as for images of single muons [5–8]. This has two consequences: On the one hand the arrival time structures across the observed Cherenkov shower image, from pixel to pixel, depend on the type of the primary particle. On the other hand, also the recorded Cherenkov pulse shape inside an individual pixel depends on the primary particle. To exploit the pulse shape differences, an ultra-fast digitization of the Cherenkov pulses is necessary, as is provided by the most recent upgrade of the data acquisition of the MAGIC telescope to a

2 GSamples/s FADC system [9,10]. This paper, however, deals with the signal reconstruction of the data taken with the initial 300 MSamples/s FADC system. Because of its limited sampling speed, we do not try to exploit the differences in pulse shape here.

This paper is structured as follows: In Section 2 the read-out system of the MAGIC telescope is described, and in Section 3 the average pulse shapes of calibration and cosmic pulses are reconstructed, from data taken with the FADC system. These pulse shapes are compared to those implemented in the MC simulation program. In Section 4 criteria for an optimal signal reconstruction are developed. In Section 5 the signal reconstruction algorithms and their implementation in the MAGIC software framework (MARS [11]) are described. The performance of the signal extraction algorithms under study is assessed by applying them to pedestal, calibration and MC events (Sections 6–8). Section 9 gives the CPU-time requirements for the different signal reconstruction algorithms. Finally in Sections 10 and 11 the results are summarized and an outlook is given.

2. Signal read-out

Fig. 1 shows a sketch of the MAGIC read-out system, including the PMT camera, the analog-optical link, the majority trigger logic and FADCs. The response of the PMTs to sub-ns input light pulses shows a full-width at half-maximum (FWHM) of 1.0–1.2 ns and rise and fall times of 600 and 700 ps correspondingly [12]. A transmitter using a vertical-cavity surface-emitting laser (VCSEL) diode modulated in amplitude, converts the electrical pulse supplied by the PMT into an optical signal. This signal is then transferred via optical fibers (162 m long, $50/125\,\mu\text{m}$ diameter) to the counting house [13]. After transforming the light back to an electrical signal, the original PMT pulse has an FWHM of about 2.2 ns for a single photo-electron pulse, and rise and fall times of about 1 ns.

In order to sample this pulse shape with the 300 MSamples/s FADC system, the original pulse is electronically shaped by effectively folding it with a function of 6 ns FWHM. In order to increase the dynamic range of the read-out, the signals are split into two branches, with gains differing by a factor 10. The low-gain branch is delayed by 55 ns and both branches are multiplexed and read out by one FADC. The switch from high- to low-gain occurs only if the high-gain signal exceeds a pre-set threshold, and 55 ns after this happens. During the subsequent 50 ns the low-gain signal is connected to the output while the high-gain signal is blocked. Fig. 2 shows the average reconstructed pulse shape (generated by a fast pulser, see Section 3) as measured by one FADC. A more detailed overview about the MAGIC read-out and DAQ system can be found in Ref. [14].
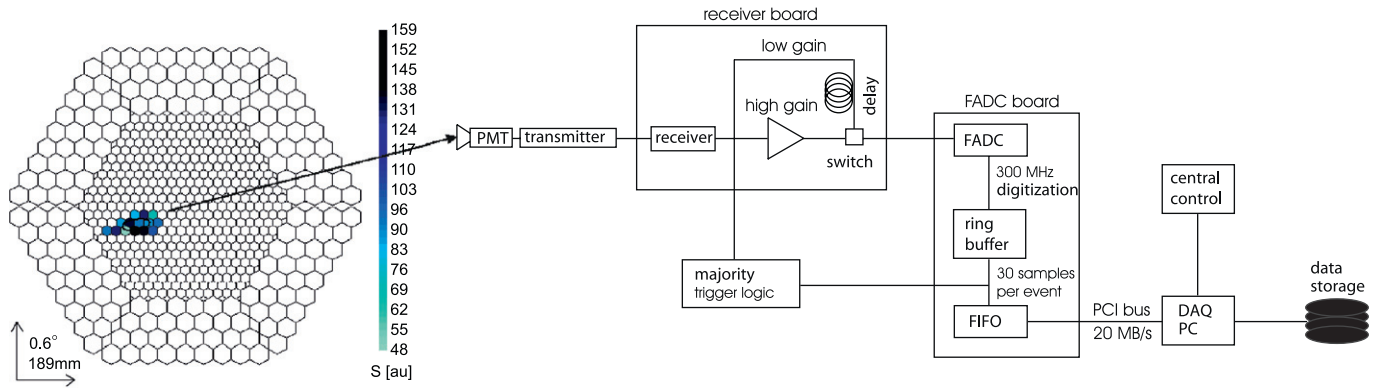
Fig. 1. MAGIC read-out scheme: the analog PMT signals are transferred via an analog optical link to the counting house where—after the trigger decision—the signals are digitized by a 300 MHz FADCs system and written to the hard disk of a data acquisition PC.
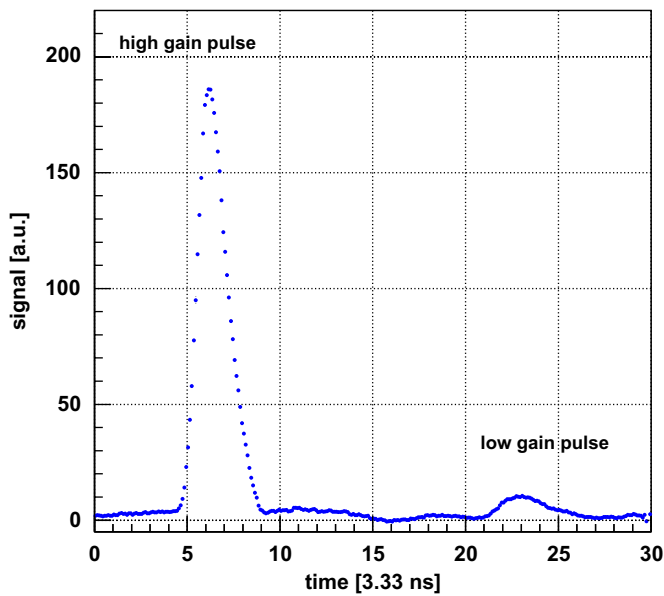
Fig. 2. Average reconstructed pulse shape from a fast pulse generator showing the high-gain and the low-gain pulse. The FWHM of the high-gain pulse is about 6.3 ns while the FWHM of the low-gain pulse is about 10 ns.

The following intrinsic characteristics of the MAGIC read-out system are the most important ones to affect the signal reconstruction:

Inner and outer pixels: The MAGIC camera is constructed with two types of pixels, inner and outer pixels, with the following differences:

(1) Size: The outer pixels have an area larger than the inner pixels by a factor of 4 [15]. Their area multiplied by photon detection efficiency, however, is higher only by a factor of 2.6.
(2) Gain: The camera is flat-fielded in order to yield a similar reconstructed charge signal in all pixels, for the same photon illumination intensity. In order to achieve this, the gain of the inner pixels has been adjusted to about a factor of 2.6 higher than the outer ones [16]. This results in a lower charge RMS contribution from the LONS for the outer pixels.
(3) Delay: Due to the lower high voltage (HV) settings of the outer pixels, their signals are delayed by about 1.5 ns with respect to the inner ones.

Asynchronous trigger: The FADC clock is not synchronized with the trigger. Therefore the time t_{rel} between the trigger decision and the first read-out sample is uniformly distributed along the range $t_{rel} \in [0, T_{FADC}]$, where $T_{FADC} = 3.33$ ns is the digitization period of the MAGIC 300 MHz FADCs. All FADCs run at the same frequency and phase. The 300 MHz clock signal is produced at a central place, multiplicated and distributed by equally long cables to the individual FADC modules.

AC coupling: The PMT signals are AC-coupled at various places in the signal transmission chain. Thus the contribution of the PMT pulses due to the LONS is on average zero. Only the signal RMS depends on the intensity of the LONS. In moonless nights, observing an extra-galactic source, an average background rate of about 0.13 photo-electrons per nano-second per inner pixel has been measured [9].

Shaping: As already mentioned above, the optical receiver board shapes the pulse with a shaping time of 6 ns FWHM, i.e. much larger than the typical intrinsic pulse width. Since the shaping time is larger than the width of a single FADC slice, a strong correlation of the noise between neighboring FADC slices is expected.

3. Pulse shape

The fact that the signal pulses are sampled asynchronously by the FADCs allows one to determine the average pulse shape with high accuracy. To do that, the signal samples from different recorded pulses are shifted to a common reconstructed arrival time and normalized to a common area/charge. Therefore, the precision of the determination of each point along the pulse shape depends on the accuracy of the arrival time and charge reconstruction. Possible biases in the charge and arrival time reconstruction may introduce systematic errors, whose sizes are unknown at the first hand. Fig. 2 shows the average signal from a fast pulser as reconstructed by the MAGIC read-out system. The relative statistical error of the amplitude value of every reconstructed point is well below 10^{-2}. The pulser generates unipolar pulses of about 2.5 ns FWHM and with a preset amplitude. These electrical pulses are fed to the VCSEL transmitters, and are transmitted using the same analog-optical link as the PMT pulses, and are fed into the MAGIC receiver board. Fig. 3 (left) shows the normalized average pulse shape for the pulse generator in the high and in the low-gain, respectively. The intrinsic FWHM of the generated pulses is 2.5 ns, whereas it is on average 6.3 and 10 ns for the pulses reconstructed from the high- and low-gain chains, respectively. The broadening of the low-gain pulses with respect to that of the high-gain ones is due to the limited bandwidth of the passive 55 ns on-board delay line of the MAGIC receiver boards.
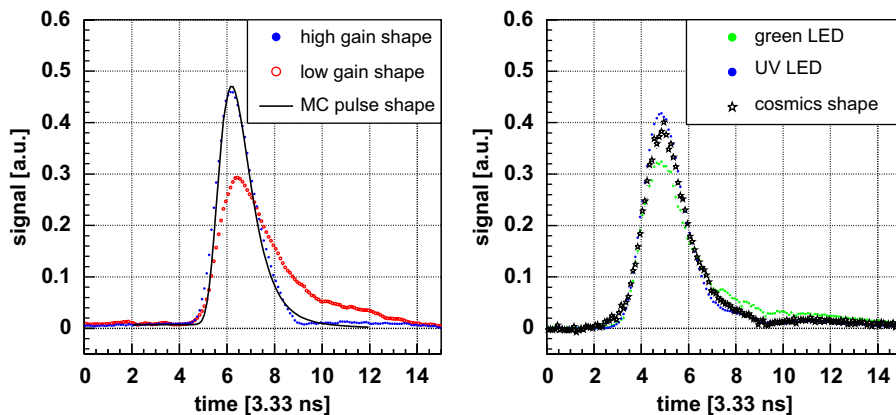
Fig. 3. Left: Average reconstructed high-gain and low-gain pulse shapes from a pulse generator run. The black line corresponds to the pulse shape implemented into the MC simulations [17]. Right: Average reconstructed high-gain pulse shape for calibration runs with green and UV light (see Section 8). All pulse shapes are normalized to a common arrival time and area.

Fig. 3 (right) shows the normalized average reconstructed pulse shapes for green and UV calibration LED pulses [18] (see Section 8) as well as that of cosmic events. The shapes of the UV calibration and cosmic pulses are quite similar. Both have an FWHM of about 6.3 ns. Since air showers from hadronic cosmic rays trigger the telescope much more frequently than γ-ray showers, the reconstructed pulse shape of the cosmic events corresponds mainly to hadron induced showers. The pulse shape from electromagnetic air showers might be slightly different as indicated by MC simulations [6,5]. The pulse shape for green calibration LED pulses is wider and has a pronounced tail. The difference between the shapes of the calibration LED pulses is not due to the LED light color but due to different electronics used for the fast LED drivers.

The reconstructed pulse shapes for generator pulses, cosmic and calibration events permit to implement a representative pulse shape in the MC simulations, see e.g. the full black line in Fig. 3, left panel. The shape difference between the calibration pulses and the cosmic pulses has to be corrected in the calibration procedure [16].

4. Criteria for optimal signal extraction

The goal of the optimal signal reconstruction algorithm is to compute an unbiased estimate of the charge and arrival time of the Cherenkov pulse with the highest possible resolution. Let us consider a large number of identical signals, corresponding to a fixed number of photo-electrons N_{phe}. By applying a signal extraction algorithm, a distribution of estimated signals $\widehat{N_{phe}}$ is obtained, see also Ref. [19] and references therein. Criteria for an optimal signal reconstruction algorithm are developed according to Ref. [20]. The deviation between true and reconstructed value is given by

$$X = \widehat{N_{phe}} - N_{phe}. \tag{1}$$

The distribution of X has a mean B (the *bias* of the estimator) and a variance V. The parameter B is also called the *bias* of the estimator and RMSE is the *root mean-squared error* which combines resolution and bias:

$$\mathrm{RMSE} \equiv \sqrt{\langle X^2 \rangle} = \sqrt{V + B^2}. \tag{2}$$

Generally, both B and RMSE depend on N_{phe} and the background fluctuations BG. In the case of the MAGIC telescope, the background fluctuations are due to the electronics noise and the PMT

response to the LONS. The signals from the latter have the same shape as those from Cherenkov pulses. Therefore, those algorithms which search for the highest sum of a number of consecutive FADC slices inside a global time window (so-called *sliding window algorithms*) will have a bias. In case of no Cherenkov signal they will typically reconstruct the largest noise pulse. Nevertheless, such a sliding window algorithm usually has a much smaller variance and in many cases a smaller RMSE than the *fixed window extractors*, which just sum up a fixed number of FADC slices. The reconstructed charge should be proportional to the total number of photo-electrons in the PMT. This linearity is very important for the reconstruction of the shower energy and hence for the measurement of energy spectra from astronomical sources. Deviations from linearity may be caused in different ways: at very low signals, the signal will be biased towards too high values (positive X). At very high signals, the FADC system goes into saturation, and the reconstructed signal becomes too low (negative X). Also, any error in the inter-calibration between the high- and low-gain acquisition channels yields an effective deviation from linearity.

Another important feature of an extractor is its robustness, i.e. its stability in reconstructing the charge and arrival time for different types of pulses with different intrinsic shapes and background levels:

- Cherenkov signals from γ-rays, hadrons and muons;
- calibration pulses from different LED color pulsers (with different pulse shapes, see Fig. 3 right panel);
- pulse generator pulses.

Finally, the extractor has to accurately reconstruct both the high- and low-gain channels. Due to the analog delay line, the low-gain pulse is wider. The total recorded time window is relatively small, such that parts of the low-gain pulse may lie outside of the recorded FADC window.

5. Signal reconstruction algorithms

We have chosen four algorithms for the study of the reconstruction of the signal charge and arrival time: fixed window, sliding window with amplitude-weighted time, cubic spline with integral or amplitude extraction, and digital filter. For the signal reconstruction algorithms adopted by other air Cherenkov telescopes, see e.g. Refs. [21,22,8,23].

5.1. Fixed window

This signal extraction algorithm simply adds the pedestal-subtracted FADC slice contents of a fixed range (window) of consecutive FADC slices. The window has to be chosen large enough to always cover the complete pulse, otherwise physical differences in the pulse position with respect to the FADC slice numbering would lead to integration of different parts of the pulse. For this reason, the fixed window algorithm adds up more noise than the other considered signal reconstruction algorithms. Due to the AC-coupling of the read-out chain, the reconstructed signals have no bias.

In the current implementation, the fixed window algorithm does not calculate arrival times.

5.2. Sliding window with amplitude-weighted time

This signal extraction algorithm searches for the maximum integral content among all possible FADC windows of fixed size contained in a defined time range (global window). The arrival time is calculated from the window with the highest integral as

$$t = \frac{\sum_{i=i_0}^{i_0+\mathrm{ws}-1} s_i \cdot t_i}{\sum_{i=i_0}^{i_0+\mathrm{ws}-1} s_i} \tag{3}$$

where i denotes the FADC slice index, starting from slice i_0 and running over a window of size ws. The s_i are the pedestal-subtracted FADC slice contents and the t_i are the corresponding times relative to the first recorded FADC slice.

5.3. Cubic spline with integral or amplitude extraction

This signal extraction algorithm interpolates all the pedestal-subtracted FADC slice contents of the full read-out window using a cubic spline algorithm, adapted from Ref. [24]. In a second step, it searches for the position of the maximum of the interpolation function. Thereafter, two different estimators of the pulse charge are available:

(1) *Amplitude*: the value of the spline maximum is taken as reconstructed signal.
(2) *Integral*: The interpolation function is integrated in a window of fixed size, with integration limits fixed with respect to the position of the spline maximum.

The pulse arrival times can also be estimated in two ways:

(1) *Pulse maximum*: The position of the spline maximum determines the arrival time.
(2) *Pulse half maximum*: The position of the half maximum at the rising edge of the pulse determines the arrival time.

5.4. Digital filter

The goal of the digital filtering method [25,26] is to optimally reconstruct the charge and arrival time of a signal whose shape is known. Thereby, the noise contributions to the amplitude and arrival time reconstruction are minimized, see also Ref. [27,37]. For the digital filtering method to work properly, two conditions have to be satisfied:

- The normalized signal shape has to be constant.
- The noise properties must be constant, i.e. the noise is stationary and independent of the signal amplitude.

As the pulse shape in MAGIC is mainly determined by the artificial shaping on the optical receiver board, the first assumption holds to a good approximation for all pulses with intrinsic signal widths much smaller than the shaping constant. Also the second assumption is satisfied to a good approximation: signal and noise are independent and the measured pulse is a linear superposition of the signal and noise contributions. LONS conditions.

Let $g(t)$ be the normalized signal shape (e.g. from Fig. 3), E the signal integral (charge) and τ the shift between the timing of the physical and the considered/probed signals. Then the time dependence of the signal is given by $y(t) = E \cdot g(t - \tau) + b(t)$, where $b(t)$ is the time-dependent noise contribution. For small time shifts τ the time dependence can be linearized. Discrete measurements y_i of the signal at times t_i ($i = 1, \ldots, n$) have the form $y_i = E \cdot g_i - E\tau \cdot \dot{g}_i + O(\tau^2) + b_i$, where $\dot{g}(t)$ is the time derivative of the signal shape, $g_i = g(t_i)$ and $b_i = b(t_i)$. The correlation of the noise contributions at times t_i and t_j can be expressed by the noise auto-correlation matrix

$$\mathbf{B}: B_{ij} = \langle b_i b_j \rangle - \langle b_i \rangle \langle b_j \rangle \tag{4}$$

whose elements can be obtained from pedestal data (see Section 7). The noise auto-correlation matrix is dominated by LONS pulses shaped by 6 ns FWHM. The absolute scale of the matrix elements depends on the LONS level. The normalized matrix elements may change by about 10% due to varying LONS levels in typical observation conditions. The noise auto-correlation in the low-gain channel cannot be determined from data. The low-gain channel read-out is only activated in case the high-gain signal is above a certain threshold resulting in a measurable low-gain signal. It has to be retrieved from Monte-Carlo studies instead.

For a given pulse, E and $E\tau$ can be estimated from the n FADC measurements $\mathbf{y} = (y_1, \ldots, y_n)$ by minimizing the deviation between the measured and the known pulse shape, and taking into account the known noise auto-correlation, i.e. minimizing the following expression (in matrix form):

$$\chi^2(E, E\tau) = (\mathbf{y} - E\mathbf{g} - E\tau\dot{\mathbf{g}})^{\mathrm{T}} \mathbf{B}^{-1} (\mathbf{y} - E\mathbf{g} - E\tau\dot{\mathbf{g}}) + O(\tau^2). \tag{5}$$

This leads to the following solution:

$$E = \mathbf{w}_{\mathrm{amp}}^{\mathrm{T}}(t_{\mathrm{rel}})\mathbf{y} + O(\tau^2), \quad \mathbf{w}_{\mathrm{amp}}(t_{\mathrm{rel}})$$
$$= \frac{(\dot{\mathbf{g}}^{\mathrm{T}}\mathbf{B}^{-1}\dot{\mathbf{g}})\mathbf{B}^{-1}\mathbf{g} - (\dot{\mathbf{g}}^{\mathrm{T}}\mathbf{B}^{-1}\mathbf{g})\mathbf{B}^{-1}\dot{\mathbf{g}}}{(\mathbf{g}^{\mathrm{T}}\mathbf{B}^{-1}\mathbf{g})(\dot{\mathbf{g}}^{\mathrm{T}}\mathbf{B}^{-1}\dot{\mathbf{g}}) - (\dot{\mathbf{g}}^{\mathrm{T}}\mathbf{B}^{-1}\mathbf{g})^2} \tag{6}$$

$$E\tau = \mathbf{w}_{\mathrm{time}}^{\mathrm{T}}(t_{\mathrm{rel}})\mathbf{y} + O(\tau^2), \quad \mathbf{w}_{\mathrm{time}}(t_{\mathrm{rel}})$$
$$= \frac{(\mathbf{g}^{\mathrm{T}}\mathbf{B}^{-1}\mathbf{g})\mathbf{B}^{-1}\dot{\mathbf{g}} - (\mathbf{g}^{\mathrm{T}}\mathbf{B}^{-1}\dot{\mathbf{g}})\mathbf{B}^{-1}\mathbf{g}}{(\mathbf{g}^{\mathrm{T}}\mathbf{B}^{-1}\mathbf{g})(\dot{\mathbf{g}}^{\mathrm{T}}\mathbf{B}^{-1}\dot{\mathbf{g}}) - (\dot{\mathbf{g}}^{\mathrm{T}}\mathbf{B}^{-1}\mathbf{g})^2} \tag{7}$$

where t_{rel} is the time difference between the trigger decision and the first read-out sample, see Section 3. Thus E and $E\tau$ are given by a weighted sum of the discrete measurements y_i with the weights for the amplitude, $w_{\mathrm{amp}}(t_{\mathrm{rel}})$, and time shift, $w_{\mathrm{time}}(t_{\mathrm{rel}})$, plus $O(\tau^2)$. To reduce $O(\tau^2)$, the fit can be iterated using $g(t_1 = t - \tau)$ and the weights $w_{\mathrm{amp/time}}(t_{\mathrm{rel}} + \tau)$ [25]. Fig. 4 shows examples of digital filter weights. The expected contributions of the noise to the error of the estimated amplitude and timing only depend on the shape $g(t)$, and the noise auto-correlation $\mathbf{B}$. The corresponding analytic expressions can be found in Ref. [25].

6. Monte-Carlo studies

Pulses of a specific number of photo-electrons can be simulated by using the Monte-Carlo technique to simulate signal pulses and noise (for the MAGIC MC simulations, see Ref. [17]). Moreover, using MC, the same pulse can be studied with and without added noise. In the subsequent studies, the
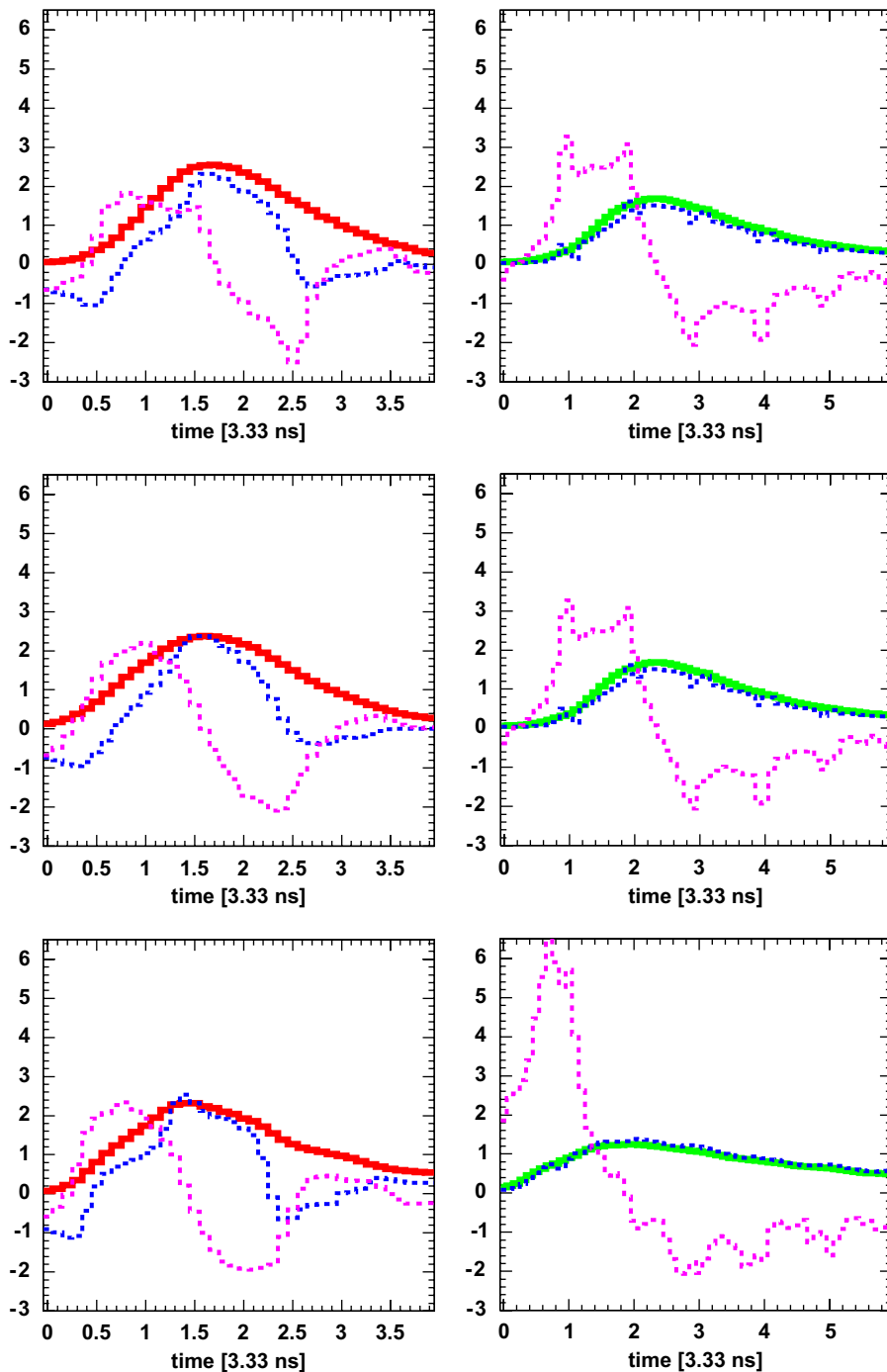
Fig. 4. Examples of digital filter weights. Top: cosmic pulses, center: UV calibration pulses and bottom: blue and green calibration pulses. On the left side, the high-gain pulse is shown, one the right side, the low-gain. Full lines show the normalized signal shapes $g(t)$ (multiplied by 5 for better visibility), dashed lines the amplitude weights $w_{amp}(t)$, and dotted-dashed lines the time weights $w_{time}(t)$. For the high-gain extraction 4 FADC slices are used and for the low-gain extraction 6 FADC slices.

Monte-Carlo simulation was used to determine, for each of the tested extractors, the following quantities: the bias and the charge resolution as functions of the input signal charge. For the subsequent studies, the following settings have been used:

- The LONS level in the MC simulations has been set to the value determined from extra-galactic source observation conditions (0.13 photo-electrons per ns, see Ref. [9]).
- The electronics noise has been simulated without any correlations between the FADC samples as a Gaussian distribution

with a sigma of 1.6 FADC counts (corresponding to about 0.2 photo-electrons) per FADC slice, roughly at the level measured in data. Note, that in the data the electronic noise introduces a correlation between the FADC samples.
- The intrinsic arrival time spread of the photons was set to be 1 ns (FWHM of a Gaussian), as expected for γ-ray showers.
- The conversion factor from photo-electrons to integrated charge over the whole pulse was set to 7.8 FADC counts per photo-electron.
- The relative timing between the trigger and the signal pulse was uniformly distributed over 1 FADC slice.

• The total dynamic range of the entire signal transmission chain was set to infinite, thus the detector has been simulated to be completely linear.

6.1. Bias

The signals were simulated with noise and extracted using the different extractor algorithms. For all sliding window algorithms the extraction window was allowed to move 5 FADC slices, independently of its size. For each signal extraction algorithm the average conversion factor between the reconstructed charge in FADC counts and the input number of photo-electrons was determined separately. The signal reconstruction bias was calculated as a function of the simulated number of photo-electrons N_{sim}:

$$B = \langle \hat{N}_{rec} - N_{sim} \rangle. \tag{8}$$

Fig. 5 shows the results for some tested extractors, with different initializations. As expected, the fixed window extractor does not show any bias up to statistical precision. All other extractors, however, do show a bias. Usually, the bias vanishes for signals above 5 photo-electrons, except for the sliding window. In this latter case, the bias only vanishes for signals above 12 photo-electrons.

6.2. Root-mean-square error

In order to obtain the precision of a given extractor, we calculated the relative RMSE:

$$\text{Rel.RMSE} = \frac{1}{N_{sim}} \sqrt{\text{Var}[\hat{N}_{rec}] + B^2}. \tag{9}$$

Fig. 6 shows the relative RMSE for the high-gain and low-gain parts separately. Also the square root of the relative variance of the number of simulated photo-electrons ($\sqrt{1/N_{sim}}$) is shown, which corresponds to the intrinsic fluctuations of the signal from air showers, following Poissonian statistics. Note, that the PMT introduces an additional excess noise [28], which is on average 18% of the Poissonian fluctuations for the MAGIC PMTs. For all extractors the variance of the reconstructed signal is dominated by noise and only slowly increases with rising signals due to mis-reconstruction of the signal pulse itself. Therefore, the relative RMSE is proportional to $1/N_{phe}$. For small numbers of photo-electrons, extractors with small extraction windows or the digital filter yield the smallest values of RMSE, but the difference is only important below about 5 photo-electrons. Above that value, the curves for all extractors have crossed the black line, i.e. they are more precise than the intrinsic fluctuations of the signal. This is also true for the entire low-gain extraction range. The best results are obtained with the digital filter or a spline integrating 1 FADC slice.

7. Pedestal extraction

The pedestal is the average FADC count for the signal baseline (no input signal). To determine the pedestal setting off-line,
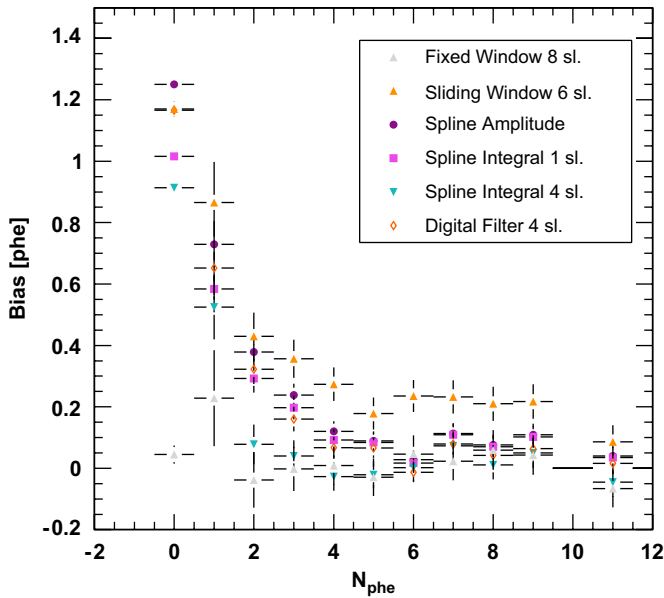
Fig. 5. Charge reconstruction bias as a function of the number of generated photo-electrons from MC simulations including electronic noise plus LONS. Above 12 photo-electrons, the bias vanishes for all signal extractors.
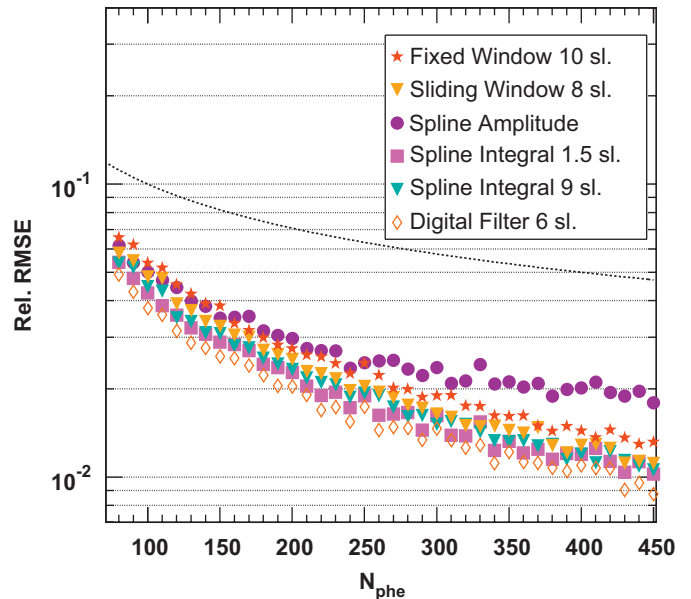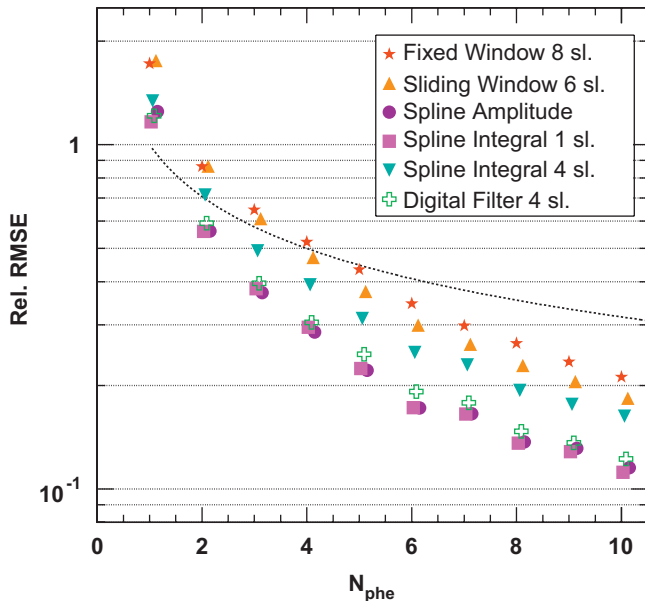
Fig. 6. Relative RMSE as a function of the number of generated photo-electrons from MC simulations including fully simulated electronic noise plus LONS. Left: high-gain, right: low-gain. The black dashed line shows the square root of the relative variance of the incoming numbers of photo-electrons, note, that the PMT introduces an additional excess noise [28]. The best results are obtained with the digital filter or a spline integrating 1 FADC slice.

Table 1
The statistical parameters square root of reconstructed signal variance, bias, RMSE and $N_{phe}^{thres.}$ for the tested signal extractors, applied to pedestal events

Name	Closed camera			MC simulation			Extra-galactic LONS				Galactic LONS			
	$\sqrt{\mathrm{Var}[N_{rec}]}$	B	RMSE	$\sqrt{\mathrm{Var}[N_{rec}]}$	B	RMSE	$\sqrt{\mathrm{Var}[N_{rec}]}$	B	RMSE	$N_{phe}^{thres.}$	$\sqrt{\mathrm{Var}[N_{rec}]}$	B	RMSE	$N_{phe}^{thres.}$
Fixed window 8	1.2	**0.0**	1.2	2.1	**0.0**	2.1	2.5	**0.0**	2.5	7.5	3.0	**0.0**	3.0	9.0
Sliding window 2	0.5	0.4	0.6	1.1	1.0	1.5	1.4	1.2	1.8	5.4	1.6	1.5	2.2	6.1
Sliding window 4	0.8	0.5	0.9	1.4	1.1	1.8	1.9	1.2	2.2	6.9	2.3	1.6	2.8	7.5
Sliding window 6	1.0	0.4	1.1	1.8	1.0	2.1	2.2	1.1	2.5	7.7	2.7	1.4	3.0	9.5
Sliding window 8	1.3	0.4	1.4	2.1	0.8	2.2	2.5	1.0	2.7	8.5	3.2	1.4	3.5	10.0
Spline amplitude	**0.4**	0.4	0.6	1.1	1.1	1.6	1.2	1.3	1.8	4.9	1.4	1.6	2.1	5.8
Spline integral 1	**0.4**	0.3	**0.5**	1.1	0.8	1.4	1.2	1.0	1.6	4.6	**1.3**	1.3	1.8	5.2
Spline integral 2	0.5	0.3	0.6	1.2	0.9	1.5	1.4	0.9	1.7	5.1	1.6	1.2	2.0	6.0
Spline integral 4	0.7	**0.2**	0.7	1.3	0.8	1.5	1.7	**0.8**	1.9	5.3	2.0	1.0	2.2	7.0
Spline integral 6	1.0	0.3	1.0	1.7	0.8	1.9	2.0	**0.8**	2.2	6.8	2.5	**0.9**	2.7	8.4
Digital filters 4	**0.4**	0.3	**0.5**	1.0	1.3	1.6	**1.1**	0.9	**1.4**	**4.2**	**1.3**	1.1	**1.7**	**5.0**
Digital filters 6	0.5	0.4	0.6	1.1	1.3	1.7	1.3	1.3	1.8	5.2	1.5	1.5	2.1	6.0

All units are in reconstructed numbers of photo-electrons, statistical uncertainty: about 0.1 photo-electrons. The extractors yielding the smallest values for each column given in bold.

dedicated pedestal runs are used, during which the MAGIC read-out is triggered randomly. The fluctuations of the signal baseline are due to electronics noise and LONS fluctuations. Thus the pedestal RMS is a measure for the total noise level.

By applying the signal extractor to pedestal events, the bias B and the RMSE for the case of no signal ($N_{phe} = 0$) can be determined. Table 1 shows the bias, the square root of the variance Var[N_{rec}] and the root-mean-square error for randomly triggered pedestal events with closed camera and sample observations outside the Galactic plane ("extra-galactic LONS", 0.13 photo-electrons/ns) as well as within the Galactic plane ("galactic LONS"). In addition, Table 1 shows the corresponding values from MC simulations. The Var[N_{rec}] of the MC simulations is slightly lower then in the sample observations outside the Galactic plane, although the simulated LONS level in the MC simulations has been adjusted to the "extra-galactic LONS". This is in part due to neglecting the correlation of the FADC slices from the electronic noise, see Section 6. Every extractor window had the freedom to move 5 FADC slices, i.e. the global window size was fixed to five plus the extractor window size. One can see that the bias typically decreases and the variance increases with increasing sliding window size, except for the digital filter. The extractor with the smallest RMSE is the digital filter fitting 4 FADC slices with an RMSE of 1.4 and 1.7 photo-electrons for an extra-galactic and a galactic star-field, respectively.

In the so-called image cleaning [4] only the camera pixels above a certain charge threshold are used for the image parameterization [3]. The charge threshold is adjusted such that the probability of being a noise fluctuation does not exceed a certain value. For the sake of comparison, a typical value of 3σ (0.3% probability) was chosen here and that number approximated with the formula:

$$N_{phe}^{thres.} \approx B + 3\sqrt{V}. \tag{10}$$

$N_{phe}^{thres.}$ is shown in the 11th and 15th column of Table 1. Most of the sliding window algorithms yield a smaller signal threshold than the fixed window, although the former ones have a bias.

The lowest threshold of only 4.2 photo-electrons for the extra-galactic star-field and 5.0 photo-electrons for the galactic star-field is obtained with the digital filter fitting 4 FADC slices. This is almost a factor of 2 lower than the fixed window results.

8. Calibration

In this section, tests are described which were performed using light pulses of different color, shape and intensity produced by the MAGIC LED calibration pulser system [16]. Such a system is able to provide fast light pulses of 2–4 ns FWHM, with intensities ranging from 3 to more than 600 photo-electrons in one inner PMT of the MAGIC camera. These pulses can be produced in three colors: green, blue and UV. Table 2 lists the available colors and intensities.

Although the pulse shape of the UV LEDs is very stable from event to event, the green and blue LED pulses can show smaller secondary pulses about 10–40 ns after the main pulse. Note that the UV-pulses are only available in intensities that do not saturate the high-gain read-out channel. However, the brightest combination of (blue) light pulses easily saturates all high-gain channels of the camera, but does not saturate the low-gain read-out.

8.1. Number of photo-electrons

The mean number of photo-electrons $\langle \hat{N}_{phe} \rangle$ was calculated for a sequence of calibration pulses of same intensity, following the excess noise factor method [28] and using different signal extractor algorithms. If the signals are extracted correctly, $\langle \hat{N}_{phe} \rangle$ should be independent of the signal extractor.

In our case, an additional complication arises from secondary pulses of the green and blue colored light pulses, which may introduce a dependence of $\langle \hat{N}_{phe} \rangle$ on the extraction time-window size (recall Fig. 3). For the standard MAGIC calibration procedure [16] only UV calibration pulses are used. Fig. 7 shows $\langle \hat{N}_{phe} \rangle$ for the standard UV calibration pulse. The results differ by less than 5%, which results in an additional systematic error to the absolute energy scale of the reconstructed events. Note that the total systematic uncertainty of the absolute energy scale was estimated to be 16% [29]. A small increase in $\langle \hat{N}_{phe} \rangle$ for an increasing window size can be observed. This may be due to the intrinsic time structure of the calibration pulse.

The peak-to-peak variation of the conversion factor between FADC counts and number of photo-electrons for the different intensities is below 10% [30] for all extractors. The corresponding

Table 2
The pulser colors available from the calibration system

Color	Wavelength (nm)	Spectral width (nm)	Min. no. Phe's	Max. no. Phe's	Secondary pulses	FWHM pulse (ns)
Green	520	40	6	120	yes	3–4
Blue	460	30	6	600	yes	3–4
UV	375	12	3	50	no	2–3
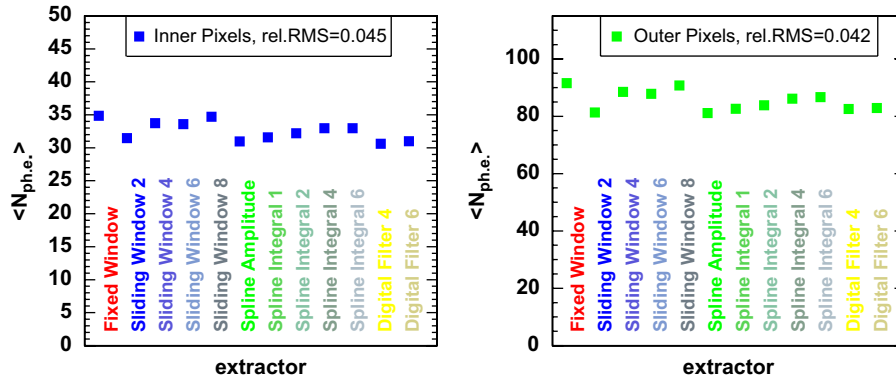
Fig. 7. $\langle \hat{N}_{phe} \rangle$ from the standard calibration pulse, emitted by 10 UV LEDs, reconstructed with different signal extractors. Left: inner pixels, right: outer pixels. The statistical errors are smaller than the marker size.

Table 3
Pulse form dependency of integration windows

Window size (FADC slices around maximum)	High gain				Low gain	
	MC	Cosmic	Calib. UV	Calib. Blue	Cosmic	Calib. Blue
Amplitude	5.4	5.0	4.5	4.1	3.4	2.5
1 slice	54	50	46	41	35	27
2 slices	78	76	71	66	60	48
4 slices	97	98	95	89	90	82

Shown is the fraction of the signal (in percent of the complete pulse integral), contained in different time windows around the pulse maximum for different pulse shapes. In the case of the first line "Amplitude", the signal amplitude has simply been divided by the complete pulse integral (arbitrary units).

non-linearity is due to the intrinsic non-linearity of the MAGIC signal chain and a possible non-linear signal extraction.

8.2. Robustness tests

Possible *variations of the pulse shape* may degrade the signal extraction quality of the MAGIC data. Variations of the pulse form have a physical reason: average Cherenkov pulses from hadronic showers are usually broader than those from electromagnetic cascades. Additionally there are differences between the pulse form of calibration pulses and those of cosmic pulses. These variations mainly affect those signal extractors which integrate only parts of a pulse or perform fits to a sample pulse form. In order to quantify the magnitude of the effect, Table 3 lists the fraction of the pulse which is contained in typical time windows around the pulse maximum, for various pulse forms. While the amplitude extraction or integration of only 1 FADC slice around the maximum yield differences as high as 10% (cosmic-c–UV), the error is reduced to about 3% if 4 FADC slices are being integrated. Further deviations, characterized by the blue LED calibration pulse or the MC pulse, yield an even stronger discrepancy.

The digital filtering method assumes a constant signal shape to compute the weight functions. In fact, all pixels are assumed to

have the same average signal shape and the same weights are used for all pixels. In order to test the robustness of the digital filtering method with respect to deviations of the actual pulse shape from the assumed pulse shape, the standard UV calibration pulse was extracted using different weight functions (computed for UV and blue calibration pulses, Cherenkov pulses and the low gain). The results are displayed in Fig. 8 showing variations of about 8% in the reconstructed signal for typical pulse form variations (blue, UV and cosmic weights) and 3% in $\langle \hat{N}_{phe} \rangle$ after calibration using the same weights. Note, photons from a γ-ray shower (from a weighted spectrum) arrive within 2–2.5 ns [5].

In conclusion, an event-to-event variation of the pulse shape may cause a charge reconstruction error of up to 10% for all signal extractors which do not integrate the entire pulse. The size of this error decreases with increasing integration window size. For the digital filter this event-to-event variation of the pulse shape may lead to an error of the reconstructed signal of up to 8%. A systematic difference in the pulse shape causes an error of up to 3% (after calibration) in the case of the digital filter.

8.3. Time resolutions

The calibration light pulses can be used to test the time resolution of signal extractors. Thereby, the arrival time difference
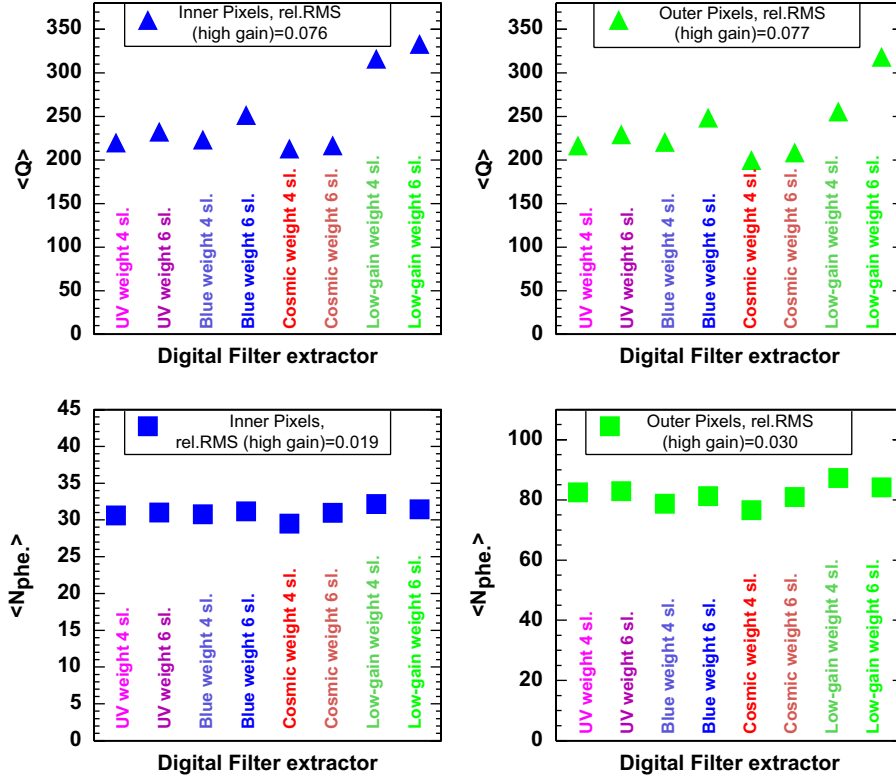
Fig. 8. Mean reconstructed charge in FADC counts (top) and $\langle \hat{N}_{\text{phe}} \rangle$ (bottom) from a standard calibration pulse reconstructed with a digital filter using different weight functions (computed for UV and blue calibration pulses, Cherenkov pulses and the low gain). Left: inner pixels, right: outer pixels. The relative RMS was calculated for the first six (high-gain) pulse forms. The statistical errors are smaller than the marker size.

δt is measured for every channel, with respect to a reference channel:

$$\delta t_i = t_i - t_{\text{ref}} \tag{11}$$

where t_i denotes the reconstructed arrival time of pixel number i and t_{ref} the reconstructed arrival time of a reference pixel. Using a calibration run of a fixed number of calibration pulses, the mean and RMS of the distribution of δt_i for a given pixel can be computed. The RMS is a measure of the combined time resolutions of pixel i and the reference pixel. Assuming that the photomultipliers and read-out channels are of the same kind, an approximate time spread of pixel i is obtained from the sigma of a Gaussian fit to the distribution of the time differences δt_i:

$$\Delta t_i \approx \sigma(\delta t_i)/\sqrt{2}. \tag{12}$$

Fig. 9 shows the obtained average time resolutions $\langle \Delta t_i \rangle$ as a function of $\langle \hat{N}_{\text{phe}} \rangle$ for various calibration runs taken with different colors and light intensities for the telescope pointing outside the Galactic plane ("extra-galactic LONS", 0.13 photo-electrons/ns). Three time extractors were used: a sliding window of 6 FADC slices with amplitude-weighted time, the cubic spline with the position of the half-maximum at the rising edge of the pulse as arrival time and the digital filter. Note that a time resolution of more than 1 ns can be obtained for all pulses above a threshold of 5 photo-electrons. For the largest signals, a time resolution as good as 200 ps can be obtained. In order to understand the exact behavior of the time resolution, we briefly review the main contributions:

(1) The intrinsic arrival time spread of the photons on the PMT: This time spread can be estimated roughly by the intrinsic width δt_{IN} of the input light pulse. The resulting time resolution is given by

$$\Delta t \approx \frac{\delta t_{\text{IN}}}{\sqrt{N_{\text{phe}}}}. \tag{13}$$

The width δt_{IN} is about 1 ns for γ-ray pulses, a few ns for hadron pulses, for muons a few hundred ps and about 2–4 ns for the calibration pulses.

(2) The transit time spread δt_{TTS} of the photo-multiplier (the spread of the times between the release of an electron from the photo cathode and the corresponding signal at the PMT output) which can be of the order of a few hundred ps per single photo-electron, depending on the wavelength of the incident light. As in the case of the photon arrival time spread, the total time spread scales with the inverse of the square root of the number of photo-electrons:

$$\Delta t \approx \frac{\delta t_{\text{TTS}}}{\sqrt{N_{\text{phe}}}}. \tag{14}$$

(3) The reconstruction error due to the background noise and limited extractor resolution:

$$\Delta t \approx \frac{\delta t_{\text{rec}} \cdot R/\text{phe}}{N_{\text{phe}}} \tag{15}$$

where $R = \sqrt{\text{Var}[\hat{N}_{\text{phe}}]}$ is the square root of the extractor variance, which depends only very weakly on the signal charge.

(4) A constant offset due to the residual FADC clock jitter between different channels or the MC simulation time steps:

$$\Delta t \approx \delta t_0. \tag{16}$$
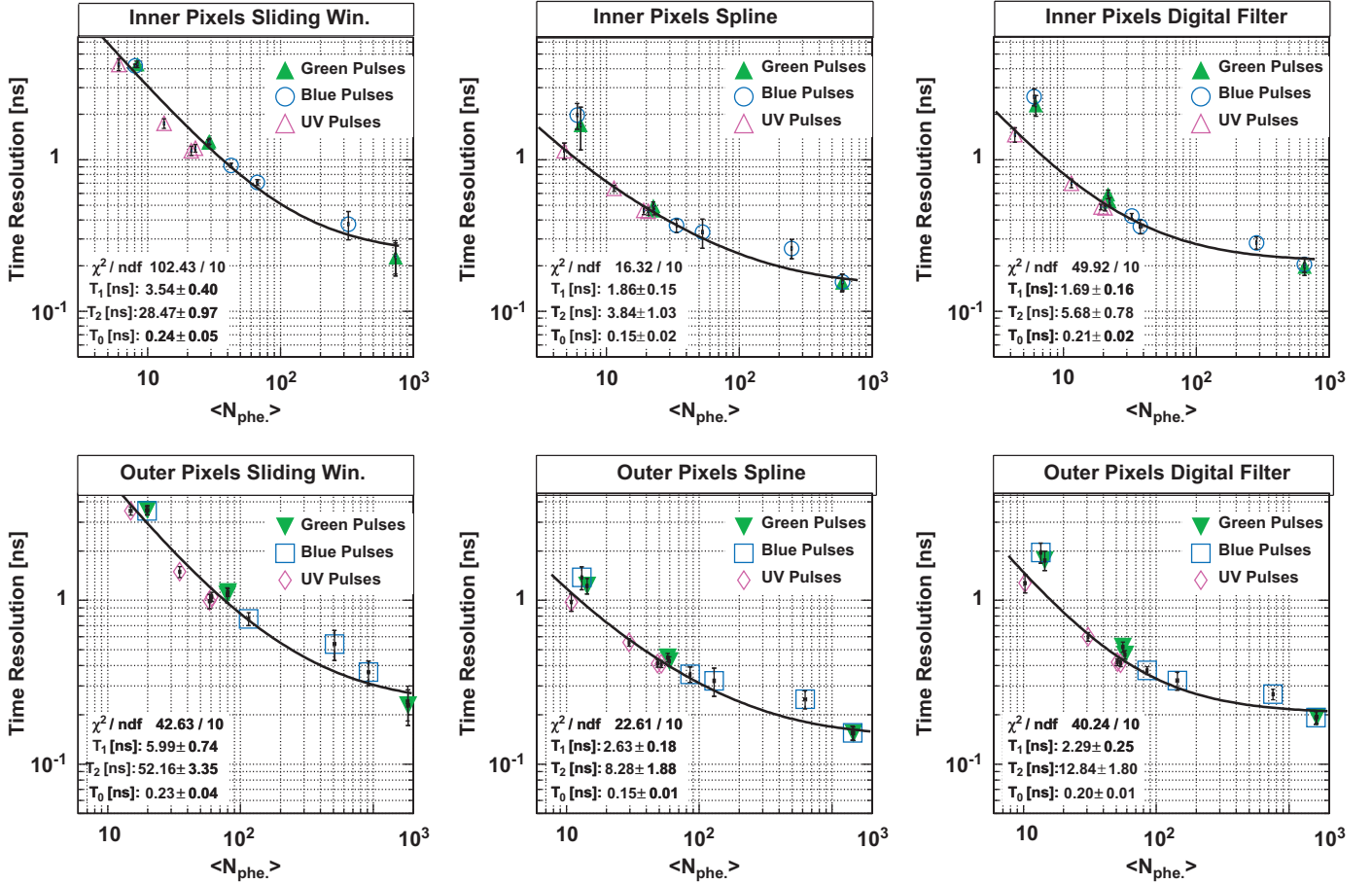
Fig. 9. Reconstructed mean arrival time resolution as a function of the extracted mean number of photo-electrons for three different extractors: the amplitude-weighted sliding window with a window size of 6 slices (left), the half-maximum searchingspline (center), and the digital filter with correct pulse weights over 6 slices (right). Error bars denote the spread (RMS) of time resolutions of the investigated channels. The marker colors show the applied pulser color, except for the last (green) point where all three colors were used. The lines are a fit using (Eq. (17)), see text for details. The best fit parameters are shown as an inset.

In total, the time spread can be expressed as

$$\Delta T = \sqrt{\frac{T_1^2}{N_{phe}} + \frac{T_2^2}{N_{phe}^2} + T_0^2} \qquad (17)$$

where T_1 contains the contributions of δt_{IN} and δt_{TTS}, the parameter T_2 contains the contribution of δt_{rec} and T_0 the offset δt_0.

The measured time resolutions in Fig. 9 were fitted by Eq. (17). The low fit probabilities are partly due to the systematic differences in the intrinsic pulse shapes of the different color LED light pulses. Nevertheless, all calibration colors had to be included in the fit to cover the full intensity range. In general, the time resolutions for the UV pulses are systematically better than those for the other colors. This can be attributed to the fact that the UV pulses have a smaller intrinsic pulse width [30] and the UV LEDs are very stable from event to event, whereas the green and blue LED pulses can show secondary pulses about 10–40 ns after the main pulse (see Section 8.1), which influence the reconstructed pulse arrival time.

There are clear differences between the studied time extractors, especially the sliding window extractor yields poorer resolutions. This is in part due to the fact that in the chosen sliding window algorithm the bias of the time reconstruction with respect to the relative timing (phase) of the pulses with respect to the free running FADC clock has not been corrected for. The parameters T_1 and T_0 should in principle be independent of the

time extraction algorithm. Nevertheless, T_1 is larger for the sliding window algorithm than for the spline interpolation and the digital filter. This is in part due to the (anti-)correlation between the reconstructed charge and arrival time for the former extractor, see Eq. (3).

From the measured time resolution for calibration pulses one can estimate the expected time resolution for cosmic pulses. The only important difference between calibration and cosmic pulses are different arrival time spreads of the photons on the PMT camera. The time spread of the photons on the PMT for cosmic pulses is smaller than for blue/green calibration pulses, but about the same as for the UV calibration pulses (see the widths of the pulses in Fig. 3b).[2] Therefore, the timing resolution for cosmic pulses is at least at the level of the timing resolution determined from the calibration pulses. The timing resolution for cosmic pulses is conservatively estimated to

$$\Delta T_{cosmic} \approx \sqrt{\frac{4.5\,\text{ns}^2}{N_{phe}} + \frac{20\,\text{ns}^2}{N_{phe}^2} + 0.04\,\text{ns}^2}. \qquad (18)$$

---

[2] Note that the calibration light pulses illuminate directly the camera, whereas the cosmic light pulses are reflected by the MAGIC mirror system. The MAGIC mirrors have been built in a parabolic shape, and are thus isochronous. Nevertheless, they have been staggered in a chess-board manner [31] with an offset of about 10 cm. This introduces an additional contribution of about 700 ps width to the intrinsic arrival times spread of the Cherenkov photons.

For signal charges above 10 photo-electrons the time resolution is below 830 ps. For signals of 100 photo-electrons the time resolution may be as good as 300 ps.

9. CPU requirements

The speed of different extractor algorithms (the number of reconstructed events per unit time) was measured on an Intel Pentium IV, 2.4 GHz CPU machine. Table 4 shows the average results whereby the individual measurements could easily differ by about 20% from one try to another (using the same extractor). The numbers in this list have to be compared with the event reading and decompression speed (400 events/s). Every signal extractor being faster than this reference number does not limit the total event reconstruction speed. Only some of the integrating spline extractor configurations lie below this limit and would need to be optimized further.

10. Results and discussion

The results based on the investigations discussed above are summarized in Table 5. Note that there is no absolute basis for criteria to separate acceptable from non-acceptable properties of signal extraction algorithms. In the following the arbitrarily chosen criteria to compare the extractors are motivated:

- The extractor should yield on average the true number of photo-electrons and should not deviate by more than 10% in case of slight modifications of the pulse shape. These deviations directly effect the determination of the absolute energy scale of the reconstructed events. Note that the dominant systematic error to the absolute energy scale is currently the photon detection efficiency (10–12%) [29]. This requirement excludes extractors which integrate only a small portion of the pulse, especially the amplitude sensing cubic spline extractor.
- The extractor must yield a stable low-gain pulse extraction. This means that apart from being robust against modifications of the pulse shape, the extractor has to reconstruct on average the true signal charge also in case of variations of the pulse position within the recorded FADC samples. This criterion excludes the fixed window extractor since arrival time jitters may exceed the time window between the tail of the high-gain pulse and the beginning of the low-gain pulse.
- The RMSE of the reconstructed charge for the case of no signal should not exceed 2 photo-electrons (an arbitrarily chosen threshold) for dark night observations and the RMSE of the reconstructed charge for air shower signals should never exceed the intrinsic Poissonian signal fluctuations plus excess noise above 5 photo-electrons. Camera pixels with a signal below 5 photo-electrons are usually rejected for the image parameterization [3,4]. This low-energy analysis condition discards the large sliding windows and the fixed window extractor. It is not critical for high-energy analyses, however.
- For analyses close to the energy threshold, an extractor should have a small or negligible bias, discarding again the amplitude sensing cubic spline extractor.
- The time resolution should not be less than 2 ns at a signal strength of 10 photo-electrons. Note that this condition allowed us to require a time coincidence of 3.3 ns between neighboring pixels to reject noise signals in the image cleaning and thus allow to measure differential energy spectra down to 60 GeV [29]. All fixed window and all simple sliding window extractors are excluded by this condition.
- The needed CPU-time should not exceed the one required for reading the data into memory and writing it to disk. Unless further effort is made to speed up the integrating spline, it is excluded if used with a large integration window.

Table 5 shows which extractors satisfy the above criteria. One can see that there is no signal extractor without a problem. However, the digital filter fitting 4 FADC slices can always be used for the high-gain extraction, and the digital filter fitting 6 FADC slices for the low-gain extraction. The mean pulse position is not

Table 4
The extraction speed measured for different signal extractor configurations

Name	Events/s (CPU)
Fixed window 8 slices	3200–4000
Sliding window 6 slices	1000–1300
Spline amplitude	700–1000
Spline integral 1 sl.	300–500
Digital filter	700–900

Note that the fixed window does not calculate the arrival time.

Table 5
The tested characteristics for every extractor

Extractor configuration	Robustness pulse form high gain	Robustness pulse form low gain	RMSE	Bias	Time	Speed
Fixed window 8 sl.	OK	NO	NO	BEST	NO	BEST
Sliding window 2 sl.	NO	NO	OK	OK	NO	OK
Sliding window 4 sl.	OK	NO	NO	OK	NO	OK
Sliding window 6 sl.	OK	OK	NO	OK	NO	OK
Sliding window 8 sl.	OK	BEST	NO	OK	NO	OK
Spline amplitude	NO	NO	OK	NO	OK	OK
Spline integral 1 sl.	NO	NO	OK	OK	BEST	OK
Spline integral 2 sl.	NO	NO	OK	OK	BEST	OK
Spline integral 4 sl.	OK	NO	OK	OK	BEST	NO
Spline integral 6 sl.	OK	OK	NO	OK	BEST	NO
Digital filter 4 sl.	OK	NO	BEST	OK	OK	OK
Digital filter 6 sl.	OK	OK	OK	OK	OK	OK

See text for descriptions of the individual columns. OK means that the extractor has passed the test, NO that the extractor failed and BEST that the extractor has succeeded a particular test as best of all.

critical. This combination has been chosen as the standard extractor for all MAGIC data before April 2007 with the 300 MSamples/s FADC system. During a certain period, the pulse position was by mistake shifted with respect to the FADC read-out samples. In this case [32] the signal was reconstructed by the cubic spline algorithms integrating 1–2 FADC slices.

If efficiencies at low energies are not critical, i.e. a high-energy analysis threshold without the use of the timing information, the sliding window extractor can be used in configurations which cover the entire pulse. This extractor turnsout to be especially robust and was used for the data analysis in Ref. [33].

11. Conclusions and outlook

In this paper, different algorithms to reconstruct the charge and arrival time from the FADC read-out samples of the MAGIC telescope have been developed. These algorithms are tested using MC simulations, pedestal and calibration events. The achievable charge and arrival time resolutions are determined. A digital filter fitting 4 FADC slices in the high-gain channel and 6 FADC slices in the low-gain channel was chosen as the standard signal extraction algorithm.

Part of the difficulties to find a suitable signal extractor (reflected in Table 5) stem from the fact that the MAGIC signals are shaped just as long as to cover about 4 FADC slices. This choice, although necessary for a 300 MSamples/s FADC read-out, "washes out" the intrinsic pulse form differences between γ-ray and hadron showers, and thus prevents the analysis from using this information in the γ/hadron discrimination, see Ref. [34]. On the other side, the shaping time is not long enough to safely extract the amplitude from the (shaped) signal.

These problems will be overcome with the full analysis of data taken with the new 2 GHz FADC system in MAGIC [9,35]; for the initial results, see Ref. [36]. This system has been designed to reduce any pulse form deformation to the minimum. It can be expected that the individual pulse forms are then directly recognized as such, e.g. with a digital filter using two sample pulse forms (a γ-ray-like and a hadron-like) and discriminating between the two with the help of the calculated χ^2. These FADCs have a higher dynamic range and do not need a separate low-gain channel any more. It can be expected that the signal extraction will become more robust, besides extracting a wealth of additional information about the shower characteristics.

Acknowledgments

References

[1] C. Baixeras, (MAGIC Collab.), et al., Nucl. Instr. and Meth. A518 (2004) 188.
[2] E. Lorenz, Nucl. Phys. B (Proc. Suppl.) 114 (2003) 217.
[3] A.M. Hillas, in: Proceedings of the 19th ICRC, La Jolla, vol. 3, 1985, p. 445.
[4] D.J. Fegan, J. Phys. G 23 (1997) 1013.
[5] R. Mirzoyan, et al., Astropart. Phys. 25 (2006) 342.
[6] V.R. Chitnis, P.N. Bhat, Astropart. Phys. 15 (2001) 29.
[7] M.D. Roberts, J. Phys. G 24 (1998) 255.
[8] M. Heß, (HEGRA Collab.), et al., Astropart. Phys. 11 (1999) 363.
[9] H. Bartko, et al., Nucl. Instr. and Meth. A 548 (2005) 464.
[10] F. Goebel, et al. (MAGIC Collab.), Upgrade of the MAGIC telescope with a multiplexed fiber-optic 2GSamples/s FADC data acquisition system, in: Proceedings of the 30th ICRC, Merida, Mexico, arXiv:0709.2363, 2007.
[11] T. Bretz, R. Wagner, in: Proceedings of the 28th ICRC, Tsukuba, Japan, 2003, p. 2947.
[12] A. Ostankov, et al., Nucl. Instr. and Meth. A 442 (2000) 117.
[13] E. Lorenz, et al., Nucl. Instr. and Meth. A 461 (2001) 517.
[14] F. Goebel, et al., (MAGIC Collab.), in: Proceedings of the 28th ICRC, Tsukuba, Japan, 2003, p. 2939.
[15] J.A. Barrio, et al., (MAGIC Collab.), MPI-PhE 98-05, 1998.
[16] M. Gaug, et al., (MAGIC Collab.), in: Proceedings of the 29th ICRC, Pune, India, 2005, pp. 5–203, astro-ph/0508274.
[17] P. Majumdar, et al. (MAGIC Collab.), in: Proceedings of the 29th ICRC, Pune, India, 2005, pp. 5–203, astro-ph/0508274.
[18] T. Schweizer, et al., IEEE Trans. Nucl. Sci. NS-49 (2002) 2497.
[19] S.W. Smith, The Scientist and Engineer's Guide to Digital Signal Processing, ISBN: 0-9660176-3-3, 1997.
[20] F. James, R. Cousins, G. Cowan, Phys. Lett. B 592 (2004) 1 (Chapter 32).
[21] J. Holder, (Veritas Collab.), in: Proceedings of the 29th ICRC, Pune, vol. 5, 2005, p. 383.
[22] J. Holder, (Veritas Collab.), et al., Astropart. Phys. 25 (2006) 391.
[23] P. Cogan, (Veritas Collab.), in: Proceedings of the 30th ICRC, Merida, 2007, arXiv:0709.4208, in press.
[24] W.H. Press, et al., second ed., Cambridge University Press, Cambridge, 2002.
[25] W.E. Cleland, E.G. Stern, Nucl. Instr. and Meth. A 338 (1994) 467.
[26] A. Papoulis, Signal Analysis, McGraw-Hill, New York, 1977.
[27] H. Bartko, et al., (MAGIC Collab.), in: Proceedings of the 7th Workshop on Towards a Network of Atmospheric Cherenkov Detectors 2005, Palaiseau, France, 27–29 April 2005, astro-ph/0506459.
[28] R. Mirzoyan, E. Lorenz, in: Proceedings of the 25th ICRC, Durban, South Africa, 1997, pp. 7–265.
[29] J. Albert, (MAGIC Collab.), et al., Astrophys. J. 674 (2008) 1037.
[30] M. Gaug, Ph.D. Thesis, Universitat Autònoma de Barcelona, Barcelona, Spain, Available from: ⟨http://wwwmagic.mppmu.mpg.de/publications/theses/MGaug.pdf⟩, 2006.
[31] M. Garczarczyk, Ph.D. Thesis, University of Rostock, Available from: ⟨ http://wwwmagic.mppmu.mpg.de/publications/theses/MGarczarczyk.pdf⟩, 2006.
[32] J. Albert, (MAGIC Collab.), et al., Astrophys. J. 642 (2006) L119.
[33] J. Albert, (MAGIC Collab.), et al., Astrophys. J. 669 (2007) 862.
[34] D. Tescaro, et al., Diploma Thesis, Università di Padova, Italy, Available from: ⟨http://photon05.pd.infn.it:5210/Documents/tesi/tesiTescaro.ps.gz⟩, 2005.
[35] R. Pegna, et al., Nucl. Instr. and Meth. A 567 (2006) 218.
[36] D. Tescaro, et al. (MAGIC Collab.), in: Proceedings of the 30th ICRC, Merida, arXiv:0709.1410, 2007.
[37] C. Cojocaru, (ATLAS EMEC and HEC Collabs.), et al., Nucl. Instr. and Meth. A 531 (2004) 481.